



Atomic insights on intermixing of nanoscale nitride multilayer triggered by nanoindentation

Zhuo Chen^a, Yonghui Zheng^a, Lukas Löfler^b, Matthias Bartosik^c, Ganesh Kumar Nayak^b, Oliver Renk^a, David Holec^b, Paul H. Mayrhofer^c, Zaoli Zhang^{a,*}

^aErich Schmid Institute of Materials Science, Austrian Academy of Sciences, A-8700 Leoben, Austria

^bDepartment of Materials Science, Montanuniversität Leoben, A-8700 Leoben, Austria

^cInstitute of Materials Science and Technology, TU Wien, A-1060 Vienna, Austria

ARTICLE INFO

Article history:

Received 7 December 2020

Revised 12 May 2021

Accepted 14 May 2021

Available online 21 May 2021

ABSTRACT

Mechanical properties of nanoscale multilayer coatings are to a large extent governed by the number of interfaces and their characteristics. While for a reduced layer thickness, increasing strength and toughness values have been reported, properties degrade for layer thicknesses of just several nanometers. Here, we report on an entirely overlooked phenomenon occurring during the indentation of nanolayers, presumably explaining the degradation of properties. Nanoindentation, commonly used to determine properties of hard coatings, is found to disrupt and intermix the multilayer structure due to the deformation imposed. Detailed electron microscopy studies and atomistic simulations provide evidence for intermixing in an epitaxial transition metal nitride superlattice thin film induced by nanoindentation. The formation of a solid solution reduces the interfacial density and leads to a sharp drop in the dislocation density. Our results confirm that plastic deformation causes the microstructure instability of nitride multilayer, which may further improve our understanding of multilayer strength mechanisms.

© 2021 The Author(s). Published by Elsevier Ltd on behalf of Acta Materialia Inc.
This is an open access article under the CC BY-NC-ND license (<http://creativecommons.org/licenses/by-nc-nd/4.0/>)

1. Introduction

It is well-established that the intrinsic length scales of materials determine their performance [1]. In multilayer thin films, reducing the thickness of a single layer can increase the number of interfaces and enhance their hardness and toughness. According to this, numerous efforts have been devoted to design novel multilayers with a small bilayer thickness in order to acquire superior mechanical properties for potential applications. In general, multilayer structures with a bilayer-period thickness of just a few nanometers showed the best combination of hardness, toughness, and elastic modulus [2–9]. For instance, the results of Kim and Lin *et al.* indicate that TMN (transition metal nitride) CrN/AlN superlattice coatings with several nanometer bilayer periods exhibit a 1.6 times higher hardness value compared to their single-layered counterpart coatings [10,11]. Among the multilayer coatings, the combination of *rs*-TMN (rock-salt transition metal nitride)/*rs*-TMN with an epitaxial superlattice structure shows excellent mechanical properties [5,11,12]. The outstanding mechanical properties of

the epitaxial superlattice coating are attributed to different effects, including interface coherency strains and the modulus difference [2,5,13,14].

However, the beneficial effect of reduced bilayer thicknesses on mechanical properties is not observed for any layer spacing. It has been reported that, similar to nanocrystalline metals [15–20], the hardness and toughness of the multilayer coating decrease again when the bilayer-period thickness is reduced below a certain critical value, being on the order of a few nanometer [2–9, 11]. For TMNs multilayer, the current understanding for this degradation of properties is that component intermixing already occurs during the thin film deposition and annealing process [3,21–24]. Thereby the interface density, coherent stress fields and differences in shear modulus diminish, explaining the reduced strength levels measured. This explanation actually suggests that the thin film synthesis process limits the maximum achievable mechanical properties.

However, large-scale component intermixing can be frequently observed also by severe plastic deformation [25–28]. One may thus ask whether the deformation of the multilayer coating during nanoindentation, usually used to evaluate the mechanical properties of multilayers (hardness and elastic modulus, etc.) may also trigger component intermixing and decrease of the mechanical

* Corresponding author

E-mail address: zaoli.zhang@oeaw.ac.at (Z. Zhang).

properties. If so, the measurement itself would affect the property to be measured, which may make the experimentally determined mechanical strength far lower than the intrinsic theoretical properties. Nevertheless, this important issue remains uncertain and has never been addressed before. Since the bilayer thickness of multilayer films below the peak strength is only a few nanometers, detecting potential small-scale structural and composition variations is quite challenging. Clarifying this issue is however mandatory to develop an even stronger multilayer structure. Modern advanced transmission electron microscopy (TEM), cross-sectional focused ion beam (FIB) cutting, and large-scale atomistic simulations allow probing the atomistic origin of material properties and provide the possibility to address such fundamental questions.

In this work, the cross-sectional TEM specimen were prepared from the region beneath the indented superlattice thin film (with a bilayer period thickness of 2.5 nm) using FIB milling. Spherical-aberration (C_s)-corrected high-resolution TEM (HRTEM) was applied to characterize the possible structural and chemical composition changes from the nanoscale to the atomic-scale. Combining TEM experimental observations at multiple-scales, we find compound intermixing in an *rs*-TiN/*rs*-AlN SL (superlattice) beneath the indenter tip, while the SL remains intact in the unaffected region. This indicates that the SL intermixing process is triggered by the deformation imposed by the indenter. Together with atomistic simulations, this intermixing mechanism is validated and explored in detail. Linking the atomistic insights of our study with the macroscopic mechanical properties of the coating and understanding the intermixing process could contribute to designing even stronger coatings in the future.

2. Methods

2.1. Material fabrication

The TiN/AlN superlattice thin film ($\sim 1.5 \mu\text{m}$ total film thickness, TiN $\sim 1.7 \text{ nm}$, AlN $\sim 0.8 \text{ nm}$) was synthesized using an AJA International Orion 5 lab-scale deposition system equipped with a computer-controlled shutter system. The reactive magnetron sputtering process was carried out at 700°C (substrate temperature) in an Ar/N₂ mixed gas atmosphere with a total pressure of 0.4 Pa and an Ar/N₂ flow ratio of 7 sccm / 3 sccm. To avoid intermixing of the two-layer materials via excessive ion bombardment, we applied a rather low bias potential of -40 V (floating potential $\sim -20 \text{ V}$) to the MgO (100) substrate, just enough to obtain a dense coating morphology. The three-inch Ti and two-inch Al target were DC-powered setting constant target currents of 1.0 and 0.5 A, respectively. Further details can be found in Ref [29].

2.2. Material characterization

The nanoindentation was performed with an Ultra Micro Indentation System (UMIS, Fischer-Cripps Laboratories) equipped with a cube corner diamond tip using a maximum load of 150 mN. The maximum load depth is about 1.7 μm . The nanoindentation was carried out at a constant indentation strain rate and indents were separated from each other by at least 50 μm . Here, a total of 5 nanoindentation experiments at different positions were carried out. The FIB cutting position is chosen near the indenter tip, and cutting is along the $\langle 100 \rangle$ direction of the SL (as seen in Fig.1c). 1) A protective layer of platinum with a thickness of about 2 μm on the area of interest was deposited. Two 6 μm deep trenches were made on either side of the selected region by coarse milling at a current of 1 nA, after which the exposed vertical faces of the specimen were coarsely polished by the ion beam using a current of 500 pA.) An ion beam is used to cut off the entire bottom end

and the vertical part. Finally, transferred and welded to a copper TEM grid for fine polishing ($\pm 2^\circ$ using a current of 50 pA).

A 300 kV field emission TEM (JEOL ARM300F) equipped with double C_s -corrector was used in this study. The high-angle annular dark-field (HAADF) images in the STEM (Scanning TEM) mode use the probe convergence semi-angle of $\sim 24 \text{ mrad}$. The STEM-HAADF images were taken by an annular dark-field image detector with the inner semi-angle larger than 64 mrad. Two windowless Energy-dispersive X-ray spectroscopy (EDXS) detectors, each of which has an active area of 100 mm², are equipped on a microscope, which are very close to the specimen with a high solid angle (1.7 sr).

A 200 kV field emission TEM (JEOL2100F) equipped with an image-side C_s -corrector was used in the HRTEM study, which demonstrates a resolution of 1.2 Å at 200 kV. The aberration coefficients were set to be sufficient small under which the HRTEM images were taken under slightly over-focus conditions (close to the Scherzer defocus). The quantitative determination of the interplanar spacing was carefully carried out by fitting intensity line profiles using a Gaussian function taken from the $\langle 100 \rangle$ direction.

The point spectra of electron energy-loss spectrum (EELS) shown in Fig.3 were recorded under TEM mode with a camera length of 25 cm with a dispersion of 0.2 eV per channel. The spectra were processed in Digital Micrograph (DM version 3.42). Firstly, the background was subtracted using the power-law model. For comparison, the spectra were then aligned to the N-K edge's onset to examine the variations of N-K and T-L edges, such as the chemical shift and shape change.

STEM-EELS spectrum images were acquired using a dispersion of 0.2 eV per channel, a collection semi-angle of 10 mrad, and a convergence semi-angle of 2.5 mrad. The images were aligned to the Ti-L₃ peak and processed in DM. In the end, an energy difference map ($E_{\text{Ti-L}_2} - E_{\text{Ti-L}_3}$) is obtained using the energy of the Ti-L₂ subtracting that of the Ti-L₃, which can be used to distinguish the solid solution and layered region (shown in Fig. 3b).

For the dislocation density in Fig. 9e, a total of 15 HRTEM images of different regions (recorded at 600-800KX) are counted. Here, 5 HRTEM images are selected from each region (as-deposited, deformed SL and solid solution). In [001] zone axis, the dislocations are located along the (200) and (020) lattice planes or {220} lattice planes, respectively. All dislocations that only insert {220} lattice planes or {200} lattice planes are counted and designated as edge dislocations. For detailed statistical methods, please refer to our previous work in Ref. [30]. The dislocation density was obtained according to the following formula, $\rho = N/A$, where ρ is the dislocation density, N is the number of dislocations, A is the area.

2.3. Molecular dynamic simulations

MD simulations were performed using LAMMPS [31] and an Al-TiN MEAM potential [32]. The simulation box was created with AtomsK [33] with initial dimensions of 17.85 nm for the x, y and z axis and contains 592704 atoms. The layer thickness is according to the synthesized films and stacked along the z axis. Prior to the indentation, the energy of the cell was minimized until a difference of 10^{-5} eV was reached. As timestep 0.1 fs was chosen. The indenter was modeled by the LAMMPS fix indent and has spherical shape with a radius of 3.5 nm. This LAMMPS fix creates a virtual object exerting forces on atoms which decay with distance from the indenter center. From its starting position above the surface of the cell, the indenter was moved at a constant rate of 0.28 Å/ps in negative z direction. Every 500 time steps a snapshot of the atom positions, i.e., coordinates of each atom at the x, y, and z positions, along with forces, velocities and energies was taken.

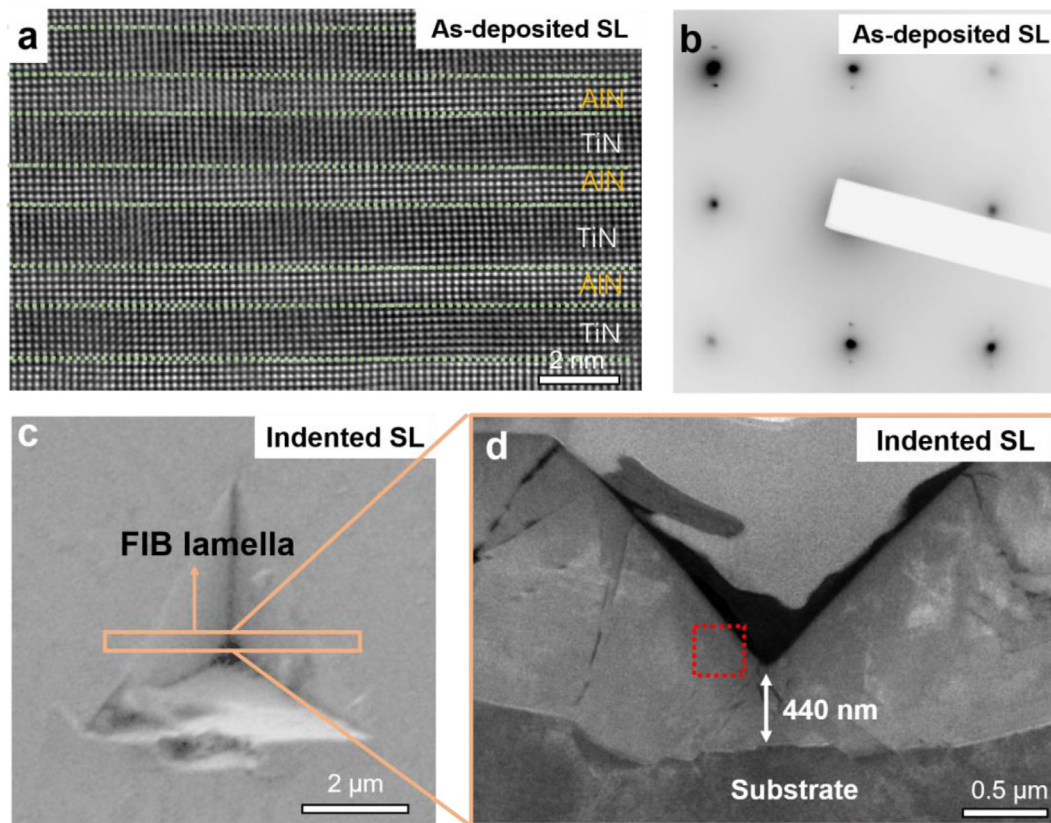


Fig. 1. **a**, Typical HRTEM image of the as-deposited *rs*-TiN/*rs*-AlN SL. **b**, Selected-area electron diffraction pattern of as-deposited SL. **c**, SEM top view of the indented SL. **d**, Cross-sectional low magnification STEM HAADF image of the indented SL with some cracks visible.

To track the state of intermixing in different regions during the indentation, the number of the atoms of the two metal species was counted for fixed volumes distributed in the simulation box. At each time step the relation between Al and Ti was calculated allowing monitoring the transition from multilayer to an intermixing. The occurring dislocations were tracked using the DAX [34] function of OVITO [35] applied to the fcc nitrogen sub lattice (as the transition metal and nitrogen atoms sit on two interpenetrating fcc lattice, the function only runs on N atom sublattices).

2.4. DFT calculation

We used density functional theory (DFT), implemented in the Vienna Ab initio Simulation Package (VASP) to estimate the barriers for diffusion governing the intermixing process [36,37]. GGA-PBE [37] was employed for the electron-electron exchange and correlation potential. The potentials used for the element Ti treat semi-core states Ti ($[Ne]3s^23p^63d^4s^2$) as valence. Ion-electron interactions were described using the projector augmented wave method [38] with a plane-wave energy cutoff of 500 eV. Supercells with 64 and 216 lattice sites yielded energies differing less than 1 meV/at., hence a supercell of 64 atoms ($a \times 2 \times 2$ supercell of conventional rock-salt structure) was used as a defect-free TiN and AlN. For these cubic supercells, a Monkhorst-Pack k-point mesh [39] of $10 \times 10 \times 10$ was used for Brillouin zone sampling with a Methfessel-Paxton [40] smearing of 0.2 eV.

The energy difference between an initial and a transition state of a jump needs to be determined to calculate its jump frequency. Each initial state was completely relaxed with respect to internal coordinates, volume, and shape. We quantitatively determined the transition state with the saddle point along the minimum en-

ergy diffusion path by a nudged elastic band (NEB) [41] method as implemented in VASP. The jumps between the initial and final states in both interstitial and vacancy-mediated cases are symmetric, hence we optimize the number of images by assuming the transition state in between. Hence, we tested five images versus three images versus single image NEB calculations for both interstitial and vacancy-mediated TiN barriers. Finding a good agreement (varying number of images lead to barrier height variations within 0.01 eV) for the remaining systems we performed a single image NEB calculation

3. Results

3.1. Superlattice intermixing during nanoindentation

The coating used here is an *rs*-TiN/*rs*-AlN superlattice deposited on a MgO (100) substrate, where the AlN layer thickness is ~ 0.8 nm, and that of the TiN layer is ~ 1.7 nm. The overall morphology of the as-deposited SL can be seen in the Supplementary Fig. 1. The HRTEM image (Fig. 1a) clearly reveals that in the SL structure, the layer with the bright contrast is AlN, while the layer with the dark contrast is TiN. Moreover, the as-deposited TiN/AlN SL (Fig. 1a) exhibits a well-defined epitaxial SL structure with a thin AlN layer stabilized in the rock-salt structure and a certain orientation relationship ($\{100\}_{TiN}/\{100\}_{AlN}$). Selected-area electron diffraction (SAED, Fig. 1b) with the superlattice spots also confirms that the periodic SL has a fully epitaxial growth of the cubic structures, indicating the excellent quality of the thin film. Fig. 1c shows a top view of the indent and the position of the FIB prepared cross-sectional TEM lamella. A low magnification image (STEM-HAADF, Fig. 1d) illustrates the overall morphology of the indented cross-

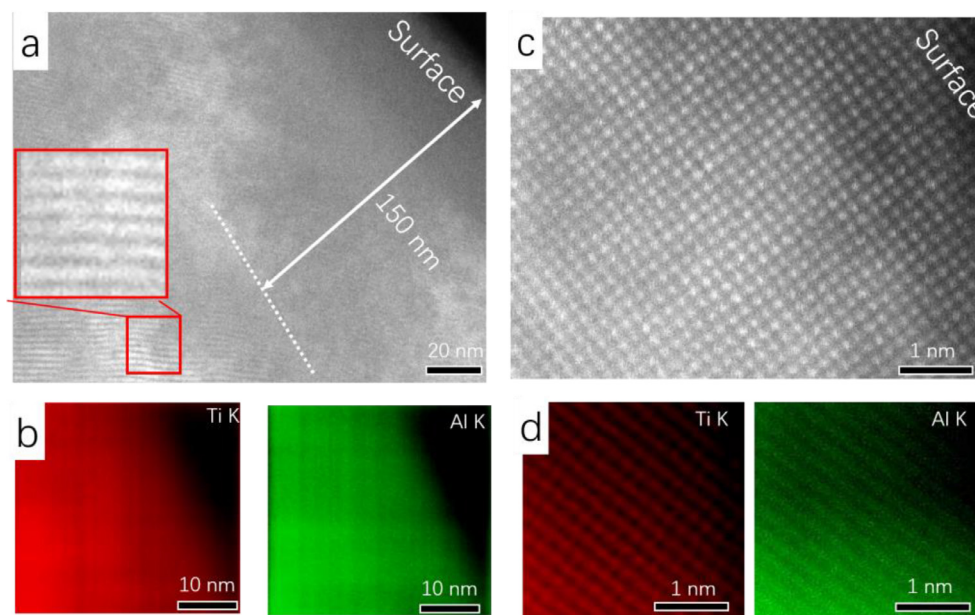


Fig. 2. **a**, Cross-sectional HAADF image of the indented SL. **b**, Overall EDXS mappings (Ti and Al K-peak signal) taken near the contact with the indenter, as indicated by the red frame in Fig.1d. **c**, **d**, Atomic-resolution HAADF and elemental mapping (EDXS) near the contact region with the indenter.

section. From the residual impression (i.e., V-shaped) of the indent, the indent depth was measured to be about 800 nm.

When focusing on very small scales of a few nanometers, an unexpected intermixing phenomenon can be detected. The high-angle annular dark-field (HAADF) image in Fig. 2a shows the morphology of the indented coating near the surface of the residual impression (see the red frame in Fig. 1d). At positions further away from the surface (~250–300 nm), the TiN/AlN SL structure is still visible, as can be seen in the inserted image in Fig. 2a. However, when moving closer to the surface of the residual impression, starting at ~150 nm away from the surface, the deposited layered morphology of the SL cannot be detected anymore. Instead, a homogeneous single-phase area has formed around the residual impression. The elemental mapping over a large area (shown in Fig. 2b) also clearly points towards a rather homogeneous chemical composition towards the surface imprint region, without any periodic chemical features of Ti or Al appearing. This strongly indicates that the deformation imposed by nanoindentation induces intermixing of the SL multilayer structure. In addition to the low magnification TEM observation of the side position of the indenter (Fig. 2a), we also performed HR-STEM/HRTEM observations in the area right below the tip of the indenter (as seen in Supplementary Figs. S2). Similarly, solid solutions with homogenous chemical compositions are still found in these areas.

Furthermore, local atomic-resolution STEM-HAADF/EDXS observations unambiguously corroborate that multilayer intermixing (element intermixing) has taken place during the indentation process. Fig. 2c shows the atomic structure image (STEM-HAADF) along the cubic [100] projection close to the surface of the residual impression, exhibiting a homogeneous distribution of image contrast, while the layered features remain absent (a HAADF image with a larger field of view is shown in Supplementary Fig. S3). Further, atomic-scale elemental mapping displayed in Fig. 2d exactly reflects that superlattice intermixing has occurred at the area close to the indenter tip. Careful inspection of the mapping reveals that Al and Ti atoms reside at identical atom column positions, which finally confirms the formation of a cubic $\text{Ti}_{1-x}\text{Al}_x\text{N}$ solid solution from the superlattice structure. Quantitative evaluation of the EDXS mapping reaches an atomic ratio between Ti and Al of 2:1 in the solid solution region (the EDXS quantitative result is obtained from

Fig. 2b and 2d), which is consistent with the atomic ratio in the as-deposited SL, i.e., 1.7 nm (8 atomic layers of TiN)/0.8 nm (4 atomic layers of AlN). Therefore, we conclude indentation induces the formation of a homogeneous single-phase $\text{Ti}_{0.66}\text{Al}_{0.33}\text{N}$ solid solution around the contact surface region. Moreover, the lattice constants vary accordingly.

In addition, the intermixing phenomenon also changes the electronic structure. Theoretical calculations revealed the influence of TMN alloying on electron density and chemical bonds [2,42–44]. Fig. 3a experimentally shows core-level EELS spectra recorded from the solid solution (the surface region) and the deformed superlattice regions (away from the surface region). The close comparison reveals that for the solid solution region, (i) the N-K (second peak) and Ti-L edges slightly shift to a higher energy position; (ii) the intensity of the first peak of the N-K edge is also relatively increased; (iii) the gap between L_2 and L_3 peaks slightly changes. The gap changes in Ti- $L_{2,3}$ edge allows further mapping of the solid solution region around the indenter. Fig. 3b displays the map of the energy difference $\Delta E = E_{L_2}^{\text{Ti}} - E_{L_3}^{\text{Ti}}$, which demonstrates the distribution of the solid solution region near the surface. Despite the small energy difference, it is still possible to visualize its distribution. As can be seen, the created solid solution zone is mainly located around the contact region of the indenter. This analysis is consistent with the HAADF observation in Fig. 2a.

3.2. Molecular dynamic simulations

The nanoindentation induced superlattice intermixing is further substantiated by extensive molecular dynamic (MD) simulations. Although the maximum indentation depth simulated by MD is only ~5.0 nm, the simulation still sheds light at the initial stages of the microstructural changes of the superlattice during the contact. In Fig. 4a, for shallow indentation depths, the MD simulation only shows the deformation of the contact layer without any noticeable intermixing behavior. When the indentation depth continues to increase (Fig. 4b), the elemental intermixing in the first two bilayers becomes obvious. The quantitative measurement results (as seen in 4d) indicate how the number of Al/Ti atoms in the evaluation boxes evolves with indentation depth. Similar to the experiments,

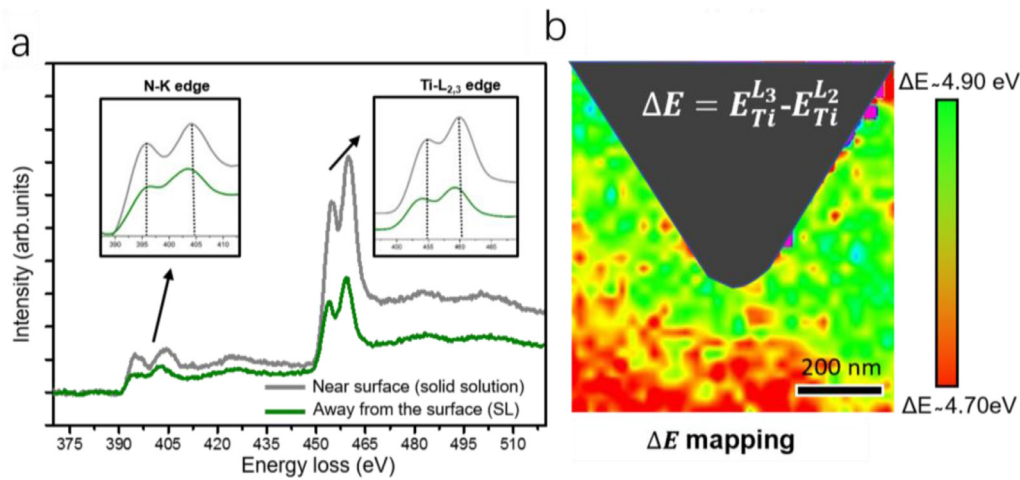


Fig. 3. **a**, EELS taken from near the surface region (solid solution) and region away from the surface, i.e., superlattice. Enlarged N-K and Ti-L edges are inserted. **b**, Mapping of the energy difference (ΔE) between Ti-L₃ and Ti-L₂. ΔE on the surface green area is approximately 4.9 eV and far away from the surface red area is approximately 4.7 eV.

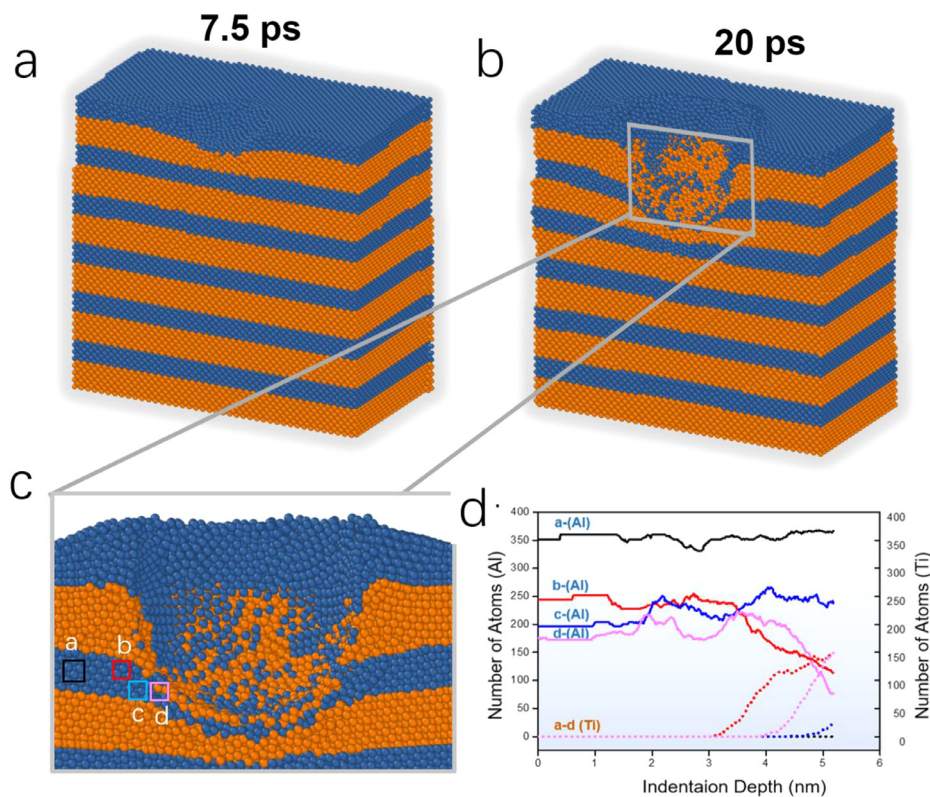


Fig. 4. **a b**, Cross-sectional view of the TiN/AlN superlattice near the indenter obtained from MD simulation (after 7.5 and 20 ps respectively). **c**, Snapshot of region next to the indenter tip (after 20 ps), where positions *a,b,c,d* are used for quantitative measurements (with a volume of $2\text{\AA} \times 2\text{\AA}$). The colored rectangles represent the positions where the atom distribution is calculated (positions *a-d*). **d**, Quantitative measurements indicating how the number of Al/Ti atoms changes with indentation depth. Solid lines represent the number change of Al atoms while dashed lines denote the number change of Ti atoms.

MD simulations reveal that the intermixing behavior largely depends on the distance from the indent. According to the atomic ratio variations of the four analyzed volumes during nanoindentation (Fig. 4d, profiles), the obvious intermixing behavior requires at least an indentation depth of more than 3 nm, reflected in the increasing Ti and decreasing Al atom numbers. For position *b* (near the interface) or position *d* (near the indenter), the intermixing is more obvious than in the analyzed volume *c* (away from the interface) or *a* (away from the indenter), but gradually diminishes when moving further away towards the unaffected volume. Therefore, our MD results demonstrate that intermixing can occur in the

affected volumes around the indenter tip, which agrees well with the experimental observations.

3.3. Superlattice intermixing mechanism

After demonstrating that intermixing occurs, the question is, how it happens during nanoindentation? Previous studies indicate that intermixing of nitride layers could occur at elevated temperatures^{31, 32, 33, 34, 35}. However, these thermally-driven diffusion phenomena only appear near the interface and no large-scale solid solution formation has been reported yet. Contrary, the observed intermixing is similar to bulk mechanical alloying observed

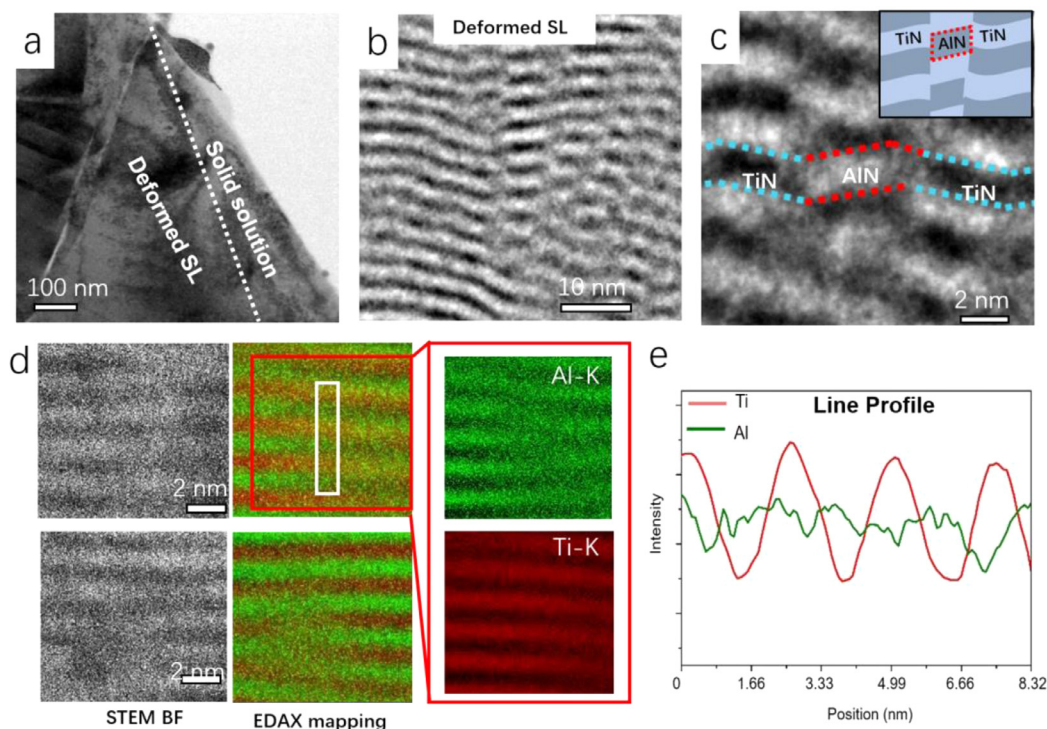


Fig. 5. **a**, TEM-BF micrograph presenting a cross-sectional overview of the imprint surface region. **b**, TEM-BF shows the deformed SL away from the imprint surface position. **c**, Enlarged BF image of the deformed SL. **d**, STEM-BF and EDXS maps at the deformed SL, with local Ti-K/Al-K maps shown on the right-hand side. **e**, The line profile is taken from the white rectangle in **d**.

due to severe plastic strains applied, e.g., during ball milling, drawing, rolling, and torsion^{24, 25, 26, 36, 37, 38, 39}. These processes were found to allow for a complete dissolution of the minority phase within the matrix, and the solubility can exceed the equilibrium value, i.e., forming a supersaturated solid solution even in an immiscible system^{24, 25, 26, 40}. However, the equivalent strains applied in the SPD process are huge compared to those realized by the cube corner indenter (i.e., ~ 20%).

Nevertheless, the observations clearly indicate that the formation of $Ti_{1-x}Al_xN$ solid solution is related to the imposed plastic deformation. A perfect solid solution is only obtained closely around the residual impression of the indenter, while moving towards the unaffected volume, the amount of the solid solution gradually reduces (supplementary Figs. S4). In this transition region a deformed TiN/AlN SL structure appears (as roughly indicated in Fig. 5a, deformed SL). The deformed SL exhibits a significant wavy-like structure (see Fig. 5b) compared to the as-deposited coating. This waviness or fragmentation of the perfect as-deposited layers could be initiated by imposed deformation during nanoindentation, as the required dislocation motion can easily create steps along the interface. Given the extremely small thickness of the multi-layer structure, these steps might be of similar height (i.e., a Burgers vector amounts up to 30 % of the layer thickness), thus easily disrupts or fragments the SL. As shown in Fig. 5d, a small piece of AlN is “broken” from the AlN layer and displaced “into” the TiN layer region. Such a tiny piece can be easily dissolved by the Gibbs-Thomson effect, similar to the process of dissolving nanoscale clusters into the matrix during SPD [25,45,46]. Thus, accompanied by the SL deformation, the intermixing of species is largely enhanced.

To further understand the intermixing process, we utilize EDXS to map elemental distribution in the deformed SL region, and DFT calculation to evaluate the migration barrier. In some positions of the deformed SL, the distinct SL structure is disrupted. The EDXS mapping (Fig. 5d) indicates that a pronounced intermixing has al-

ready occurred there, but likely with different mixing capabilities for the different species. This is clearly demonstrated in the EDXS line profiles (Fig. 5e), where Al atoms migrate across the layer, but Ti atoms do not, further proved by our atomic-scale EDXS mapping in supplementary Figs. S5. Such profiles are obviously different from those taken from the undeformed SL (supplementary Fig. S6), where no noticeable chemical intermixing is observed.

The EDXS result (Fig. 5d) suggests that the Al atom migration distance is larger than that of Ti. This observation is supported by the calculated migration energy barriers for Al in TiN and Ti in AlN. DFT results of the energy barrier variation with pressure in the case of Al in TiN, for two migration mechanisms, namely interstitial- and vacancy-mediated mechanisms are shown in Fig. 6a. Regarding Al migration in TiN (are shown in Fig. 6a), the vacancy-mediated migration is more prominent in the low-pressure condition, however, with an increase of the pressure (after ~ 14 GPa), the interstitial-mediated mechanism comes into play. Also, considering the formation energy of vacancies and interstitials in TiN (see left panel of Fig. S7), vacancies are the favored defect. For Ti migration in AlN (shown in Fig. 6b), the energy barrier exhibits a very low value (~1 eV) for the interstitial mechanism. However, the energies to form a point defect in AlN are very high: 12.89 eV and 7.64 eV for the Ti interstitial and Al vacancy, respectively (Fig. S7, right panel). Consequently, defects are expected to be very scarce and presumably make Ti migration in AlN very difficult. Al migration in TiN (vacancy mediated) is thus expected to be facilitated compared to Ti migration through AlN.

However, from a kinetic perspective, diffusion coefficients at room temperature are negligible and the diffusion distance is significantly smaller than the layer thickness (as seen in supplementary discussion). Hence, the intermixing process is most likely caused by the applied deformation driving atomic displacements during the nanoindentation process. The imposed deformation may as well activate Ti atoms (with higher energy barriers) to also mi-

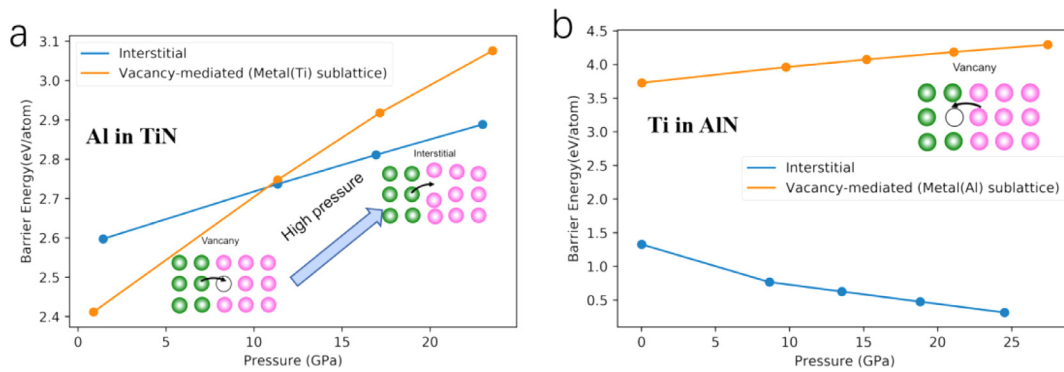


Fig. 6. **a** DFT calculations of the migration energy barrier for aluminum (Al) in titanium nitride (TiN). **b** DFT calculations of the migration energy barrier for titanium (Ti) in aluminum nitride (AlN). The blue and yellow solid lines show the pressure dependence of the energy barrier for interstitial- and vacancy-mediated mechanisms, respectively.

grate into the AlN matrix and eventually to form a uniform single-phase $Ti_{1-x}Al_xN$ solid solution (as seen Figs. 2a-d).

4. Discussion

4.1. Interface deformation-driven intermixing

When excluding enthalpy, the pressure increases the “intrinsic resistance” to atomic mixing (as DFT calculations show, Supplementary Figs. S8). However, the enthalpy contribution of the interface during plastic deformation can act as a driving force for the solid solution formation and might be large enough to overcome the positive intermixing enthalpy of solid solution [26], in particular in the case of a small bilayer period with a high density of interfaces. Our MD simulation shows no apparent intermixing behavior in the early contact of the indenter, and this stage presents a lower dislocation density (as seen in Fig. 4a and Fig. 7a). When the dislocation density is further increased (as the indentation depth increases, and so the strain in case of the spherical indenter), interface intermixing occurs (as seen in Fig. 4b and Fig. 7b). The relationship between dislocation density and intermixing behavior is clearly shown in Fig. 7c. Thus, the MD result suggests that the interface intermixing phenomenon is strongly related to the SL plastic deformation, in agreement with the experimental results. To rationalize the driving forces for the intermixing phenomenon we simply consider the total energy change of the system in the following.

The total energy of rs -TiN/ rs -AlN, E_T^{SL} , per unit (surface/interface/section) area in one bilayer period can be expressed as:

$$E_T^{SL} = t_1 \cdot E_s^{AIN} + t_2 \cdot E_s^{TiN} + t_1 \cdot E_b^{AIN} + t_2 \cdot E_b^{TiN} + E_i^{TiN/AlN} \quad (1)$$

E_s is the strain energy density (per unit volume), E_b is the bulk (chemical) energy density (per unit volume) and $E_i^{TiN/AlN}$ is the interface energy. t_1 and t_2 are the layer thicknesses of TiN and AlN, respectively ($t_1=0.8\text{nm}$ and $t_2=1.7\text{nm}$). Since the formed solid solution contains no interfaces, the total energy of cubic $Ti_{1-x}Al_xN$, E_T^{TiAIN} , per unit (surface/interface/section) area in certain thickness (2.5 nm) can be expressed as:

$$E_T^{TiAIN} = (t_1 + t_2) \cdot (E_s^{TiAIN} + E_b^{TiAIN}) \quad (2)$$

When $E_T^{TiAIN} < E_T^{SL}$, the lower total energy of the solid solution favors the intermixing process of the superlattice. However, for a given stress state, the elastic strain energy difference between the superlattice and the solid solution is negligible (see Appendix 1). Therefore, reduction or relaxation of the elastic strain energy cannot be the main driving force for intermixing. If so, plasticity would not be a prerequisite for intermixing, what is neither observed in the experiment, nor in the MD simulations.

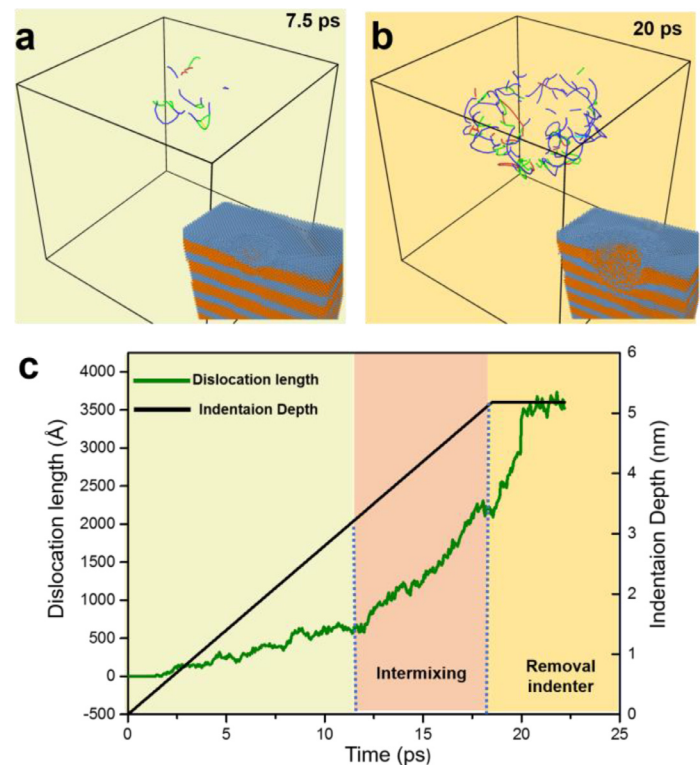


Fig. 7. **a** MD simulations showing that the number of dislocations at 7.5 ps. **b** MD simulation showing that the number of dislocations at 20 ps. Note that the dislocation network under the indenter with the green, red, and blue curved lines representing the dislocations. **c**, The development of the dislocation length (green line) during the indentation sequence in the MD simulation. Dislocations appear prior to any intermixing, and the intermixing occurs after 11 ps (from the result in Fig. 4d). The black line represents the indentation depth during the calculations.

However, plastic deformation will greatly increase the interface energy of the SL. The TEM observations demonstrate that deformation of the SL induces an evolution from a coherent interface (Fig. 8a) to an incoherent-like interface (Fig. 8b), associated with many misfit dislocations (as seen in the following section) and considerable interface steps. Accumulation of these interface dislocations may further explain the segmented appearance of the deformed superlattice. These distortions are also visible in the FFT, resulting in a broadening of the reflection spots (Fig. 8b). Such an imperfect crystallographic match at the interface significantly increases the interface energy. For instance, the rs -TMN/ rs -TMN coherent interface energy is usually less than $<20\text{meV}/\text{\AA}^2$, while the semi-coherent w -AlN/TiN(001) interface energy is already ≈ 180

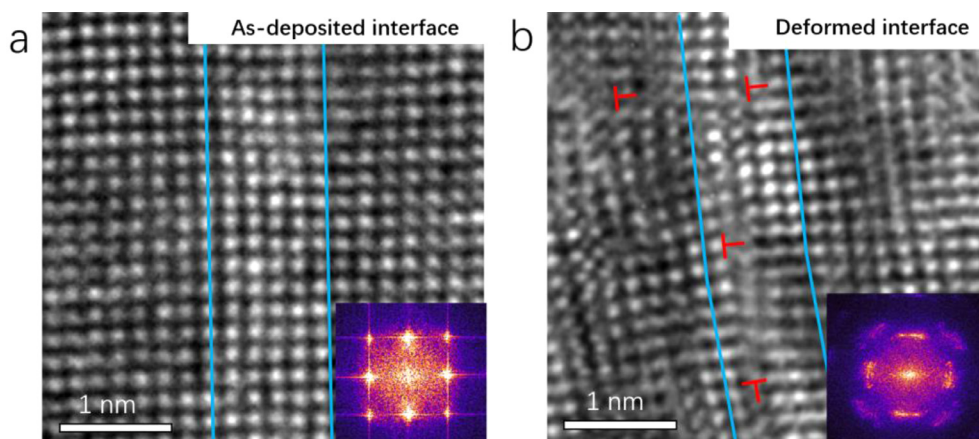


Fig. 8. **a**, HRTEM image showing the interface structure of the as-deposited SL. **b**, HRTEM image showing the interface structure of the deformed SL (after indentation). The location of the image Fig. 8b is shown in supplementary Fig. S9. Inset images of **a** and **b** show fast Fourier transform (FFT) results of HRTEM images of the as-deposited and the deformed SL.

$\text{meV}/\text{\AA}^2$ [47–49]. Thus, the plastic deformation imposed by the indenter causes a sharp increase of the interfacial energy, which can act as a main driving force for superlattice intermixing. Especially for small bilayer periods, a single-phase structure can become quite beneficial as deduced from the simple total energy balance. According to Equation 1, reducing the thickness of TiN and AlN increases the fraction of the interface energy to the total energy of the SL, while from these energetic considerations intermixing should become increasingly difficult for thicker bilayer-period coatings.

4.2. Effect of intermixing on dislocation behavior and strength

So far, three strengthening mechanisms are applied to describe variations in hardness or strength of multilayer coatings, i.e., the Hall-Petch-like strengthening relationship based on dislocations piling up at the interface [50,51], the confined layer slip (CLS) mechanism [52–54] and the interface barrier strength (IBS) mechanism [8,13,55]. Most of these models explain the hardness/strength according to the relationship between dislocations and interfaces and the respective changes if the layer volumes become confined.

For nanoscale *rs*-TMN/*rs*-TMN superlattice coatings, the mechanical strength usually increases as the bilayer period thickness decreases [2–4, 6,9,11]. This is rationalized by the interface barrier strength (IBS) mechanism, i.e., hindering dislocations crossing the interface and dislocation pile ups. For a smaller bilayer-period (less than 3–4 nm) the hardness of the multilayer coating decreases. Currently this softening is attributed to the composition mixing during the deposition process. However, our high-spatial-resolution elemental analysis clearly shows that even for the superlattice with a thickness of only 1.7 nm/0.8 nm, no apparent interface chemical intermixing and diffusion occur (as confirmed by the elemental profiles recorded from the undeformed SL region, supplementary Figs. S6). Therefore, this phenomenon is not necessarily coupled to strong interface chemical intermixing and interdiffusion during deposition.

Based on our intensive study, the strength reduction of nanoscale multilayers is somehow related to deformation triggered intermixing. After indentation, three distinct regions are identified, i.e., a solid solution region around the residual imprint, the deformed SL, and the unaffected as-deposited SL further away from the indenter (Fig.9a). The dislocation distribution between them differs significantly, as seen in Figs. 9b–d. The dislocation density (Fig.9e) in the deformed SL is quite high ($7.2\text{--}13.4 \times 10^{13}/\text{cm}^2$),

while in the solid solution region, it is relatively low ($1.0\text{--}2.8 \times 10^{13}/\text{cm}^2$), close to the value of the as-deposited SL ($0.9\text{--}1.9 \times 10^{13}/\text{cm}^2$).

We consider that dislocation densities at the imprint surface underwent a variation from a high value to a low value, as the structure transformed from the SL to the solid solution (as seen in schematic Fig.9f). For the SL, the interface is the source for nucleation and emission of many dislocations. The SL interface itself poses the dominant resistance to slip transfer across the interface [56]. However, relative to the multilayer, the solid solution formation reduces the dislocations' nucleation ability (ascribing to the disappearing of the interfacial structure) on the one hand. The creation of the uniform single-phase solid solution also increases the migration ability of dislocations on the other hand (as analyzed in Appendix 2), which causes many dislocations (generated in the stage of multilayer deformation) to migrate. These migrations include dislocation migration to the surface (annihilated on the surface), the internal multilayer structure region, and form sub-grain grain boundary, etc. In the end, a much lower dislocation density in the solid solution region than in the deformed multilayer region results, as shown in Fig.9e.

Since the solid solution region has a lower interface density and higher dislocation migration ability, it is a relatively soft region. As known, nanoindentation measured hardness of a material is often driven by the expansion of the plastic zone. The MD simulation results show that a solid solution is formed when the load depth is only about 3 nm (Figs.4). This indicates that under significant actual load conditions (i.e., the load depth of ~800 nm) both the solid solution and the multilayer may participate in the coating's plastic deformation. Thus, in our experiment (under a load of 150 mN), the resultant hardness depends on the constraint ability of the harder multilayer structure area to the softer solid solution area. At the indenter tip area, an apparent plastic deformation behavior is observed, i.e., the film/substrate interface sinking. At the indented regions, solid solution region accounts for a large portion of the total residual area (as seen in Supplementary Figs. S2). Consequently, the harder multilayer regions have weaker constraints on the softer solid solutions. We believe that the solid solution formation may improve the plastic flow under its indenter and lower the measured hardness accordingly. Meanwhile, considering that the interface energy acts as the main driving force for intermixing, a smaller bilayer-period SL facilitates alloying through the deformation. Therefore, for smaller bilayer-period TMN coatings, the effect of solid solution behavior may be more significant, which may easily lead to a decrease in its hardness. This might ex-

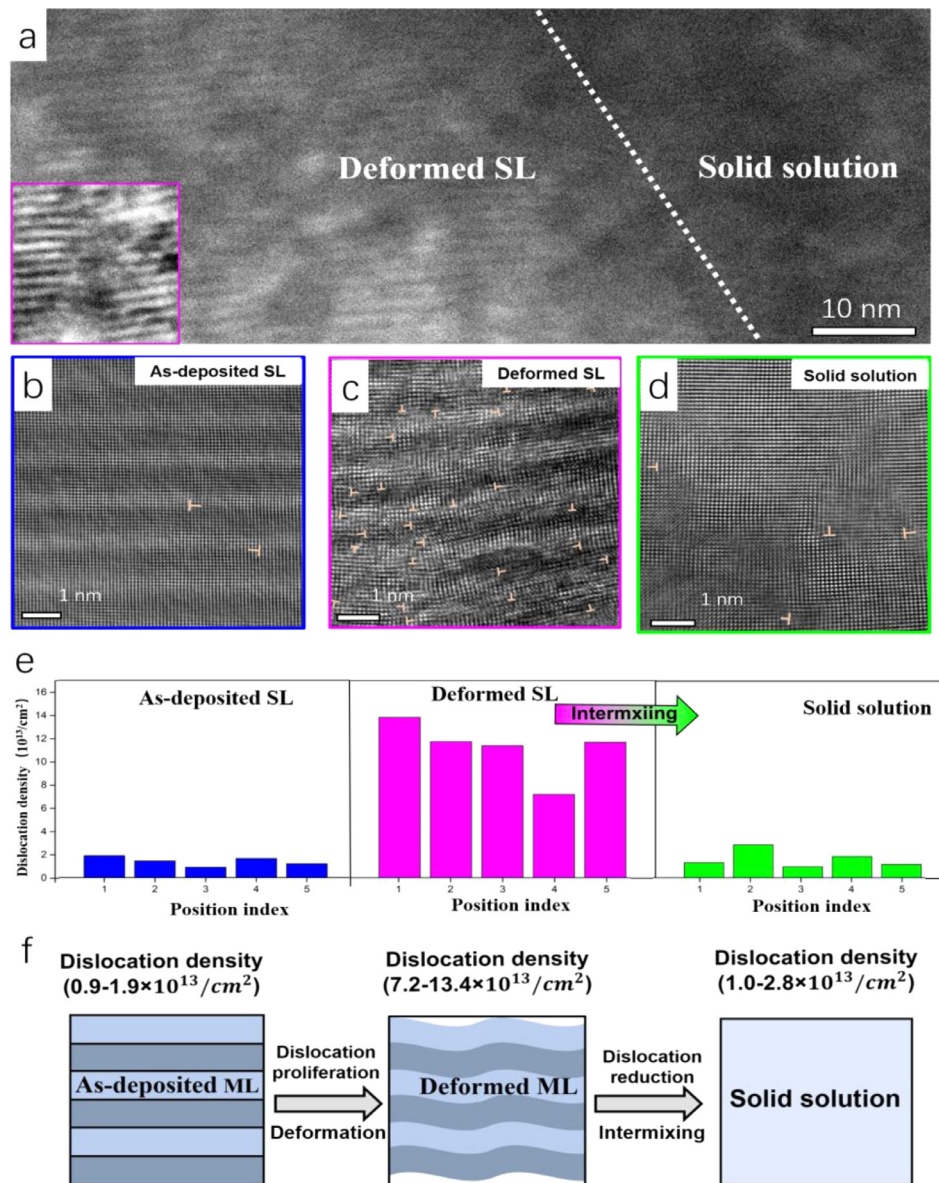


Fig. 9. **a**, HAADF image showing the distribution of solid solution and deformed multilayer regions. A locally enlarged HAADF image taken from the deformed multilayer is inserted, clearly showing its different morphology. **b, c, d**, Typical HRTEM images recorded from the as-deposited SL, deformed SL and the solid solution area. The location of the image Fig. 9a, 9c and 9d are shown in supplementary Fig. S9. **e**, Dislocation density statistics from the respective regions. **f**, Schematic illustrations of the layered structure evolution and dislocation density change from the as-deposited SL to the deformed multilayer and to the solid solution region.

plain the hardness/strength reduction in multilayer coatings when the bilayer period becomes extremely small (as seen in Fig.10).

Furthermore, our work significantly improves the understanding of the structural stability of complex nitride coating systems, such as ceramic-like $\text{Ti}_{1-x}\text{Al}_x\text{N}$ or $\text{Cr}_{1-x}\text{Al}_x\text{N}$, where the spinodal decomposition phenomenon [57-59] is the controlling mechanism to obtain superior high-temperature mechanical strength. Under practical working conditions, hard-coating tools withstand high mechanical and thermal loads. However, the current research considers only the temperature effect on structural modifications but hardly the deformation effect, which is generated in service. Our research points out that deformation may trigger the reverse process of spinodal decomposition, i.e., superlattice intermixing. Therefore, it also raises uncertainty about the strength of such complex nitride coatings under the actual load. Deformation-driven intermixing process (weaken the strength) and temperature-induced spinodal decomposition process (enhance the strength) will compete. Therefore, it requires further verification of

the structural changes under high mechanical and thermal loads for such complex nitride coatings.

5. Summary

Atomic-resolution structure and chemical composition analysis unambiguously reveal that nanoindentation cause intermixing in a nitride superlattice coating with small bilayer thicknesses, further validated by MD simulations. The observed formation of the $\text{Ti}_{1-x}\text{Al}_x\text{N}$ solid solution can be clearly related to the plastic deformation of the TiN/AlN SL imposed by nanoindentation. A single-phase solid solution is only observed near the indenter tip, while moving further away from the tip, a heavily distorted SL structure followed by a perfect unaffected SL multilayer structure can be observed. It is suggested that the coherent interfaces of the superlattice are progressively destroyed during deformation as interface dislocations accumulate. This causes a substantial rise of the interfacial energy, which provides the main driving force for

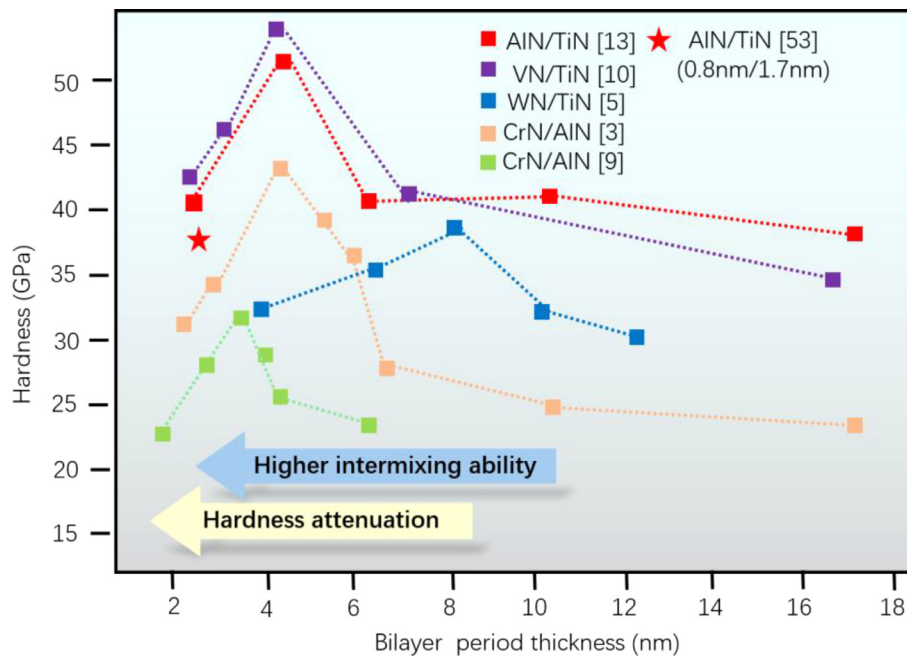


Fig. 10. A summary of hardness values plotted against the bilayer period thickness for various rock-salt/rock-salt nitride superlattices, including the present TiN/AlN (2.5 nm bilayer thickness of AlN + TiN).

multilayer intermixing. The intermixing causes a drop not only in the interface fraction but also in the dislocation densities (compared with the deformed multilayer region). Thus, our findings rationalize the mechanism responsible for the currently not well-understood strength mechanism in superlattice hard coatings with the finest bilayer thicknesses [2-9, 11].

Declaration of Competing Interest

The authors declare that they have no known competing financial interests or personal relationships that could have appeared to influence the work reported in this paper.

Acknowledgements

The financial support from the China Scholarship Council (CSC, 201608120053) for one of the authors, Z.C., is acknowledged. The authors thank M. Fallmann for the thin film synthesis and the USTEM at TU Wien for the TEM sample preparation. Financial support through Austrian Science Fund (FWF) projects number P30341-N36. (L.L., M.B. and D.H.) and I4059-N36 (G.K.N. and D.H.) are greatly acknowledged. The computational results presented have been achieved in part using the Vienna Scientific Cluster (VSC). This work is supported by FWF P 33696 (Z.Z.).

Supplementary materials

Supplementary material associated with this article can be found, in the online version, at doi:10.1016/j.actamat.2021.117004.

Appendix 1

For rs -TiN/ rs -AlN in the stage of elastic deformation, the superlattice interface will maintain a coherent state. Therefore, the change of total energy will depend on the strain energy. The strain energy density E_s corresponding to the two-dimensional bi-axial stress state for cubic materials can be expressed as:

$$E_s = \frac{1}{2}(\sigma_{11} + \sigma_{22}) \cdot \varepsilon = M\varepsilon^2 = \frac{\sigma^2}{M} \quad (3)$$

For (001) growth plane:

$$M_{(100)} = c_{11} + c_{22} - \frac{2c_{12}^2}{c_{11}} \quad (4)$$

Thus, $M_{(100)}^{TiN} = 670$ GPa, $M_{(100)}^{AlN} = 451$ GPa and $M_{(100)}^{Ti_{0.66}Al_{0.33}N} = 603$ GPa (elastic constant from the Ref. [60]). Here, assuming that SL and solid solution are under the same stress state, then the energy difference is very small. For example, if bi-axial stress of 20 GPa is introduced, the difference in strain energy in one period (2.5 nm) between superlattice and $Ti_{1-x}Al_xN$ is only 4.6 meV/A². This means the driving force for the superlattice intermixing process is insufficient if only strain energies are considered.

Appendix 2

When an interface restricts the motion of a dislocation, the dislocation at a distance x from the interface is repelled by shear stress, i.e., dislocation critical migration stress on glide planes at angle θ with the interface normal, given by the following formula [13]:

$$\tau = \frac{\alpha \Delta G b \cos \theta}{2x} \quad (5)$$

Where b is the magnitude of the dislocation Burgers vector, a is $\frac{1}{4}\pi$ for screw dislocations, and $\frac{1}{4}\pi(1-\nu)$ for edge dislocations and ν is the Poisson's ratio. ΔG is the shear modulus difference between rs -TiN and rs -AlN. When the intermixing initiates, the modulus difference between the two layers becomes smaller and eventually vanishes with formation of the homogenous solid solution. Thus, the shear stress required for the gliding of the dislocation across the interface can be significantly reduced. Further, nitride alloying also alters the 'inherent' dislocation glide ability. The alloying has the potential to lower the resistance to shear and favors dislocation glide by modifying the electronic (high valence electron concentration) effects and bonding characteristics [43,44]. Therefore, forming a solid solution changes the dislocation migration ability (increasing) and the dislocation density (reducing), which ultimately affects its yield strength [8,13,53].

References

- [1] E. Arzt, Size effects in materials due to microstructural and dimensional constraints: a comparative review, *Acta Materialia* 46 (16) (1998) 5611–5626.
- [2] J. Buchinger, N. Koutná, Z. Chen, Z. L. Zhang, P.H. Mayrhofer, D. Holec, M. Bartosik, Toughness enhancement in TiN/WN superlattice thin films, *Acta Materialia* 172 (2019) 18–29.
- [3] H.C. Barshilia, A. Jain, K.S. Rajam, Structure, hardness and thermal stability of nanolayered TiN/CrN multilayer coatings, *Vacuum* 72 (3) (2003) 241–248.
- [4] M. Schlögl, B. Mayer, J. Paulitsch, P.H. Mayrhofer, Influence of CrN and AlN layer thicknesses on structure and mechanical properties of CrN/AlN superlattices, *Thin Solid Films* 545 (Supplement C) (2013) 375–379.
- [5] R. Hahn, M. Bartosik, R. Soler, C. Kirchlechner, G. Dehm, P.H. Mayrhofer, Superlattice effect for enhanced fracture toughness of hard coatings, *Scripta Materialia* 124 (2016) 67–70.
- [6] U. Helmersson, S. Todorova, S.A. Barnett, J.E. Sundgren, L.C. Markert, J.E. Greene, Growth of single-crystal TiN/VN strained-layer superlattices with extremely high mechanical hardness, *Journal of Applied Physics* 62 (2) (1987) 481–484.
- [7] P.B. Mirkarimi, L. Hultman, S.A. Barnett, Enhanced hardness in lattice-matched single-crystal TiN/V0.6Nb0.4N superlattices, *Applied Physics Letters* 57 (25) (1990) 2654–2656.
- [8] X. Chu, S.A. Barnett, Model of superlattice yield stress and hardness enhancements, *Journal of Applied Physics* 77 (9) (1995) 4403–4411.
- [9] V. Pankov, M. Evstigneev, R.H. Prince, Room-temperature fabrication of hard AlN/TiN superlattice coatings by pulsed laser deposition, *Journal of Vacuum Science & Technology A* 20 (2) (2002) 430–436.
- [10] G.S. Kim, S.Y. Lee, J.H. Hahn, S.Y. Lee, Synthesis of CrN/AlN superlattice coatings using closed-field unbalanced magnetron sputtering process, *Surface and Coatings Technology* 171 (1) (2003) 91–95.
- [11] J. Lin, J.J. Moore, B. Mishra, M. Pinkas, W.D. Sproul, Nano-structured CrN/AlN multilayer coatings synthesized by pulsed closed field unbalanced magnetron sputtering, *Surface and Coatings Technology* 204 (6) (2009) 936–940.
- [12] M. Setoyama, A. Nakayama, M. Tanaka, N. Kitagawa, T. Nomura, Formation of cubic-AlN in TiN/AlN superlattice, *Surface and Coatings Technology* 86–87 (1996) 225–230.
- [13] J.S. Koehler, Attempt to Design a Strong Solid, *Physical Review B* 2 (2) (1970) 547–551.
- [14] N. Koutná, P. Řehák, Z. Chen, M. Bartosik, M. Fallmann, M. Černý, Z. L. Zhang, M. Friák, M. Šob, P.H. Mayrhofer, D. Holec, Correlating structural and mechanical properties of AlN/TiN superlattice films, *Scripta Materialia* 165 (2019) 159–163.
- [15] A.H. Chokshi, A. Rosen, J. Karch, H. Gleiter, On the validity of the hall-petch relationship in nanocrystalline materials, *Scripta Metallurgica* 23 (10) (1989) 1679–1683.
- [16] G.W. Nieman, J.R. Weertman, R.W. Siegel, Microhardness of nanocrystalline palladium and copper produced by inert-gas condensation, *Scripta Metallurgica* 23 (12) (1989) 2013–2018.
- [17] K. Lu, W.D. Wei, J.T. Wang, Microhardness and fracture properties of nanocrystalline NiP alloy, *Scripta Metallurgica et Materialia* 24 (12) (1990) 2319–2323.
- [18] V.Y. Gertsman, M. Hoffmann, H. Gleiter, R. Birringer, The study of grain size dependence of yield stress of copper for a wide grain size range, *Acta Metallurgica et Materialia* 42 (10) (1994) 3539–3544.
- [19] J. Schiøtz, F.D. Di Tolla, K.W. Jacobsen, Softening of nanocrystalline metals at very small grain sizes, *Nature* 391 (6667) (1998) 561–563.
- [20] P.G. Sanders, J.A. Eastman, J.R. Weertman, Elastic and tensile behavior of nanocrystalline copper and palladium, *Acta Materialia* 45 (10) (1997) 4019–4025.
- [21] H.C. Barshilia, K.S. Rajam, Raman spectroscopy studies on the thermal stability of TiN, CrN, TiAlN coatings and nanolayered TiN/CrN, TiAlN/CrN multilayer coatings, *Journal of Materials Research* 19 (11) (2004) 3196–3205.
- [22] L. Hultman, C. Engström, M. Odén, Mechanical and thermal stability of TiN/NbN superlattice thin films, *Surface and Coatings Technology* 133–134 (2000) 227–233.
- [23] P.H. Mayrhofer, C. Mitterer, L. Hultman, H. Clemens, Microstructural design of hard coatings, *Progress in Materials Science* 51 (8) (2006) 1032–1114.
- [24] H.-J. Lee, K.-W. Kwon, C. Ryu, R. Sinclair, Thermal stability of a Cu/Ta multilayer: an intriguing interfacial reaction, *Acta Materialia* 47 (15) (1999) 3965–3975.
- [25] X. Sauvage, F. Wetscher, P. Pareige, Mechanical alloying of Cu and Fe induced by severe plastic deformation of a Cu–Fe composite, *Acta Materialia* 53 (7) (2005) 2127–2135.
- [26] A. Bachmaier, M. Kerber, D. Setman, R. Pippin, The formation of supersaturated solid solutions in Fe–Cu alloys deformed by high-pressure torsion, *Acta Materialia* 60 (3) (2012) 860–871.
- [27] D. Raabe, S. Ohsaki, K. Hono, Mechanical alloying and amorphization in Cu–Nb–Ag in situ composite wires studied by transmission electron microscopy and atom probe tomography, *Acta Materialia* 57 (17) (2009) 5254–5263.
- [28] C. Suryanarayana, Mechanical alloying and milling, *Progress in Materials Science* 46 (1) (2001) 1–184.
- [29] M. Fallmann, Z. Chen, Z. L. Zhang, P.H. Mayrhofer, M. Bartosik, Mechanical properties and epitaxial growth of TiN/AlN superlattices, *Surface and Coatings Technology* 375 (2019) 1–7.
- [30] X. Gu, Z.L. Zhang, M. Bartosik, P.H. Mayrhofer, H. Duan, Dislocation densities and alternating strain fields in CrN/AlN nanolayers, *Thin Solid Films* 638 (Supplement C) (2017) 189–200.
- [31] S. Plimpton, Fast Parallel Algorithms for Short-Range Molecular Dynamics, *Journal of Computational Physics* 117 (1) (1995) 1–19.
- [32] G.A. Almyras, D.G. Sangiovanni, K. Sarakinos, Semi-Empirical Force-Field Model for the Ti1–xAlxN (0 ≤ x ≤ 1) System, *Materials* 12 (215) (2019).
- [33] P. Hirel, AtomsK: A tool for manipulating and converting atomic data files, *Computer Physics Communications* 197 (2015) 212–219.
- [34] A. Stukowski, V.V. Bulatov, A. Arsenlis, Automated identification and indexing of dislocations in crystal interfaces, *Modelling and Simulation in Materials Science and Engineering* 20 (8) (2012) 085007.
- [35] A. Stukowski, Visualization and analysis of atomistic simulation data with OVITO—the Open Visualization Tool, *Modelling and Simulation in Materials Science and Engineering* 18 (1) (2009) 015012.
- [36] G. Kresse, J. Furthmüller, Efficiency of ab-initio total energy calculations for metals and semiconductors using a plane-wave basis set, *Computational Materials Science* 6 (1) (1996) 15–50.
- [37] G. Kresse, J. Furthmüller, Efficient iterative schemes for ab initio total-energy calculations using a plane-wave basis set, *Physical Review B* 54 (16) (1996) 11169–11186.
- [38] P.E. Blöchl, Projector augmented-wave method, *Physical Review B* 50 (24) (1994) 17953–17979.
- [39] H.J. Monkhorst, J.D. Pack, Special points for Brillouin-zone integrations, *Physical Review B* 13 (12) (1976) 5188–5192.
- [40] M. Methfessel, A.T. Paxton, High-precision sampling for Brillouin-zone integration in metals, *Physical Review B* 40 (6) (1989) 3616–3621.
- [41] D. Sheppard, R. Terrell, G. Henkelman, Optimization methods for finding minimum energy paths, *The Journal of Chemical Physics* 128 (13) (2008) 134106.
- [42] D. Holec, R. Rachbauer, D. Kiener, P.D. Cherns, P.M.F.J. Costa, C. McAleese, P.H. Mayrhofer, C.J. Humphreys, Towards predictive modeling of near-edge structures in electron energy-loss spectra of AlN-based ternary alloys, *Physical Review B* 83 (16) (2011) 165122.
- [43] D.G. Sangiovanni, L. Hultman, V. Chirita, I. Petrov, J.E. Greene, Effects of phase stability, lattice ordering, and electron density on plastic deformation in cubic TiWN pseudobinary transition-metal nitride alloys, *Acta Materialia* 103 (2016) 823–835.
- [44] D.G. Sangiovanni, L. Hultman, V. Chirita, Supertoughening in B1 transition metal nitride alloys by increased valence electron concentration, *Acta Materialia* 59 (5) (2011) 2121–2134.
- [45] A.R. Yavari, P.J. Desré, T. Benamer, Mechanically driven alloying of immiscible elements, *Physical Review Letters* 68 (14) (1992) 2235–2238.
- [46] A. Bachmaier, G.B. Rathmayr, M. Bartosik, D. Apel, Z. L. Zhang, R. Pippin, New insights on the formation of supersaturated solid solutions in the Cu–Cr system deformed by high-pressure torsion, *Acta Materialia* 69 (2014) 301–313.
- [47] Z. Chen, D. Holec, M. Bartosik, P.H. Mayrhofer, Z. L. Zhang, Crystallographic orientation dependent maximum layer thickness of cubic AlN in CrN/AlN multilayers, *Acta Materialia* 168 (2019) 190–202.
- [48] A. Madan, I.W. Kim, S.C. Cheng, P. Yashar, V.P. Dravid, S.A. Barnett, Stabilization of Cubic AlN in Epitaxial AlN/TiN Superlattices, *Physical Review Letters* 78 (9) (1997) 1743–1746.
- [49] K. Yalamanchili, F. Wang, H. Aboulfadl, J. Barrirero, L. Rogström, E. Jiménez-Pique, F. Mücklich, F. Tasnadi, M. Odén, N. Ghafoor, Growth and thermal stability of TiN/ZrAlN: Effect of internal interfaces, *Acta Materialia* 121 (Supplement C) (2016) 396–406.
- [50] P.M. Anderson, C. Li, Hall-Petch relations for multilayered materials, *Nanostructured Materials* 5 (3) (1995) 349–362.
- [51] A. Misra, H. Krug, Deformation Behavior of Nanostructured Metallic Multilayers, *Advanced Engineering Materials* 3 (4) (2001) 217–222.
- [52] M.A. Phillips, B.M. Clemens, W.D. Nix, A model for dislocation behavior during deformation of Al/Al3Sc (fcc/L12) metallic multilayers, *Acta Materialia* 51 (11) (2003) 3157–3170.
- [53] A. Misra, J.P. Hirth, R.G. Hoagland, Length-scale-dependent deformation mechanisms in incoherent metallic multilayered composites, *Acta Materialia* 53 (18) (2005) 4817–4824.
- [54] J.D. Embury, J.P. Hirth, On dislocation storage and the mechanical response of fine scale microstructures, *Acta Metallurgica et Materialia* 42 (6) (1994) 2051–2056.
- [55] S.I. Rao, P.M. Hazzledine, Atomistic simulations of dislocation–interface interactions in the Cu–Ni multilayer system, *Philosophical Magazine A* 80 (9) (2000) 2011–2040.
- [56] R.G. Hoagland, T.E. Mitchell, J.P. Hirth, H. Kung, On the strengthening effects of interfaces in multilayer fee metallic composites, *Philosophical Magazine A* 82 (4) (2002) 643–664.
- [57] A. Hörling, L. Hultman, M. Odén, J. Sjöln, L. Karlsson, Mechanical properties and machining performance of Ti1–xAlxN-coated cutting tools, *Surface and Coatings Technology* 191 (2) (2005) 384–392.
- [58] P.H. Mayrhofer, F.D. Fischer, H.J. Böhm, C. Mitterer, J.M. Schneider, Energetic balance and kinetics for the decomposition of supersaturated Ti1–xAlxN, *Acta Materialia* 55 (4) (2007) 1441–1446.
- [59] A. Hörling, L. Hultman, M. Odén, J. Sjöln, L. Karlsson, Thermal stability of arc evaporated high aluminum-content Ti1–xAlxN thin films, *Journal of Vacuum Science & Technology A* 20 (5) (2002) 1815–1823.
- [60] Y. Teng, S. Zhu, F. Zhang, M. Li, F. Wang, W. Wu, Electronic structure, lattice constant, optical and mechanical properties for NaCl-structured Ti–Al–N by density functional theory, *Physica B: Condensed Matter* 358 (1) (2005) 77–85.